

# Validity of the relativistic impulse approximation for elastic proton-nucleus scattering at energies lower than 200 MeV

Z. P. Li<sup>1</sup>, G. C. Hillhouse<sup>2,1</sup>, and J. Meng<sup>1,2,3,4</sup>

<sup>1</sup>*School of Physics, Peking University, Beijing 100871*

<sup>2</sup>*Department of Physics, University of Stellenbosch, Stellenbosch, South Africa*

<sup>3</sup>*Institute of Theoretical Physics, Chinese Academy of Science, Beijing 100080 and*

<sup>4</sup>*Center of Theoretical Nuclear Physics,*

*National Laboratory of Heavy Ion Accelerator, Lanzhou 730000*

(Dated: November 10, 2018)

## Abstract

We present the first study to examine the validity of the relativistic impulse approximation (RIA) for describing elastic proton-nucleus scattering at incident laboratory kinetic energies lower than 200 MeV. For simplicity we choose a  $^{208}\text{Pb}$  target, which is a spin-saturated spherical nucleus for which reliable nuclear structure models exist. Microscopic scalar and vector optical potentials are generated by folding invariant scalar and vector scattering nucleon-nucleon (NN) amplitudes, based on our recently developed relativistic meson-exchange model, with Lorentz scalar and vector densities resulting from the accurately calibrated PK1 relativistic mean field model of nuclear structure. It is seen that phenomenological Pauli blocking (PB) effects and density-dependent corrections to  $\sigma\text{N}$  and  $\omega\text{N}$  meson-nucleon coupling constants modify the RIA microscopic scalar and vector optical potentials so as to provide a consistent and quantitative description of all elastic scattering observables, namely total reaction cross sections, differential cross sections, analyzing powers and spin rotation functions. In particular, the effect of PB becomes more significant at energies lower than 200 MeV, whereas phenomenological density-dependent corrections to the NN interaction *also* play an increasingly important role at energies lower than 100 MeV.

PACS numbers: 24.10.-i, 24.10.Ht, 24.10.Jv, 24.70.+s, 25.40.Cm, 25.60.Bx

## I. INTRODUCTION

The relativistic impulse approximation (RIA) provides an excellent quantitative description of complete sets of elastic proton scattering observables from various spin-saturated spherical nuclei at incident energies ranging from 200 to 400 MeV [1]. The latter represents the theoretical framework for generating complex microscopic optical potentials for solving the elastic scattering Dirac equation. The reliability of the RIA has also been demonstrated by the fact that, for the above energies, predictions of elastic proton scattering observables are very similar to the corresponding results based on the highly successful global Dirac phenomenological optical potentials, which have been calibrated to provide excellent quantitative predictions of elastic proton scattering observables from stable nuclei ranging from  $^{12}\text{C}$  to  $^{208}\text{Pb}$  and for incident energies between 20 and 1040 MeV [2].

The Melbourne group have already developed a highly predictive microscopic Schrödinger model for describing elastic scattering at energies between 20 and 800 MeV [3, 4]. Here, however, we focus on the RIA which is based on the relativistic Dirac equation, and is more attractive in the sense that the microscopic scalar and vector optical potentials – and consequently the corresponding Schrödinger-equivalent central and spin-orbit optical potentials [1]– are directly related to the Lorentz properties of the mesons mediating the strong nuclear force, a connection lacking in nonrelativistic models.

Recently we developed an energy-dependent Lorentz covariant parameterization of the on-shell NN scattering matrix at incident laboratory kinetic energies ranging from 40 to 300 MeV [5]. In this paper, we employ the latter meson-exchange model to generate relativistic microscopic scalar and vector folding optical potentials in order to systematically study the predictive power of the RIA for describing elastic proton-nucleus scattering observables at energies lower than 200 MeV. At these low energies of interest, multiple scattering effects [6], medium modifications of the NN interaction [3], and Pauli blocking [1, 7] contributions become increasingly important, and hence the validity of the RIA needs to be investigated at these low energies.

In Sec. (II), we briefly describe the RIA as well as the relevant input pertaining to our application thereof. Results are presented in Sec. (III), and we summarize and conclude in Sec. (IV).

## II. FORMALISM

### A. Relativistic Impulse Approximation (RIA)

A comprehensive description of the RIA, as well as the corresponding computer codes and associated numerical details can be found in Refs. [1] and [8]. Here, we just give a brief introduction of it. The Dirac optical potential is given by

$$U_{\text{opt}}(q, E) = -\frac{4\pi ip}{M} \langle \Psi | \sum_{n=1}^A e^{i\mathbf{q}\cdot\mathbf{r}^{(n)}} \hat{\mathcal{F}}(q, E; n) | \Psi \rangle \quad (1)$$

where  $p$  is the magnitude of the three-momentum of the projectile in the nucleon-nucleus center-of-mass frame,  $|\Psi\rangle$  is the  $A$ -particle ground state, and  $\hat{\mathcal{F}}$  is the nucleon-nucleon scattering operator. In the original RIA,  $\hat{\mathcal{F}}$  is chosen as:

$$\hat{\mathcal{F}}(q, E) = \sum_L F^L(q, E) \lambda_{(1)}^L \cdot \lambda_{(2)}^L \quad (2)$$

where scattering amplitudes  $F^L(q, E)$  are complex functions of the momentum transfer  $q$  and laboratory energy  $E$ , which can be obtained by the relativistic Horowitz-Love-Franey model (see section IIB), and  $\lambda_{(i)}^L$  stand for five Dirac matrices for the projectile or target nucleon.

Assuming the ground state is a Hartree product of single-particle 4-component wave functions  $U_\alpha(\mathbf{r})$ , the action of the optical potential on the incident wave  $|U_0\rangle$ , projected onto coordinate space, can be written as:

$$\begin{aligned} \langle \mathbf{r} | U_{\text{opt}}(q, E) | U_0(\mathbf{r}) \rangle &= -\frac{4\pi ip}{M} \sum_L \left[ \int d^3 r' \rho^L(\mathbf{r}') t_D^L(|\mathbf{r}' - \mathbf{r}|; E) \right] \lambda^L U_0(\mathbf{r}) \\ &\quad - \frac{4\pi ip}{M} \sum_L \left[ \int d^3 r' \rho^L(\mathbf{r}', \mathbf{r}) t_X^L(|\mathbf{r}' - \mathbf{r}|; E) \right] \lambda^L U_0(\mathbf{r}') \end{aligned} \quad (3)$$

where

$$t_D^L(|\mathbf{r}|; E) \equiv \int \frac{d^3 q}{(2\pi)^3} t_D^L(q, E) e^{-i\mathbf{q}\cdot\mathbf{r}} \quad (4)$$

with  $t_D^L(q, E) \equiv (iM^2/2E_c k_c) F_D^L(q)$  and similarly for the exchange pieces  $t_X^L(Q, E)$ . The nuclear densities are defined as:

$$\rho^L(\mathbf{r}', \mathbf{r}) \equiv \sum_i^{\text{occ}'} \bar{U}_i(\mathbf{r}') \lambda^L U_i(\mathbf{r}), \quad \rho^L(\mathbf{r}) \equiv \rho^L(\mathbf{r}, \mathbf{r}) \quad (5)$$

Here the prime on the occupied states means that one sums over target protons when the density is to be used with  $pp$  amplitudes and over target neutrons when it is to be used with  $pn$  amplitudes.

The first term in Eq. (3) contains a multiplicative factor that defines the direct optical potential:

$$U_D^L(r, E) = -\frac{4\pi ip}{M} \int d^3r' \rho^L(\mathbf{r}') t_D^L(|\mathbf{r}' - \mathbf{r}|; E) \quad (6)$$

Adopting a local-density approximation, the second term can be localized to give:

$$U_X^L(r, E) = -\frac{4\pi ip}{M} \int d^3r' \rho^L(\mathbf{r}', \mathbf{r}) t_X^L(|\mathbf{r}' - \mathbf{r}|; E) j_0(p|\mathbf{r}' - \mathbf{r}|) \quad (7)$$

where  $j_0$  is a spherical Bessel function. For spin-zero nucleus, the non-zero densities are only baryon, scalar and a tensor term associated with  $\sigma^{0i}$ . Hence, the RIA optical potential can be written as

$$U_{\text{opt}}(r; E) = U^S(r; E) + \gamma^0 U^V(r; E) - 2i\alpha \cdot \hat{\mathbf{r}} U^T(r; E) \quad (8)$$

where

$$U^L(r; E) = U_D^L(r; E) + U_X^L(r; E) \quad (9)$$

These optical potentials serve as input to solve the Dirac equation for elastic proton scattering so as to generate the relevant partial-wave scattering phase shifts for computing the scattering observables, namely the total reaction cross section  $\sigma_R$ , the differential cross section  $d\sigma/d\Omega$ , analyzing power  $A_y$  and spin rotation function  $Q$ . Similar to Ref. [1], we resolve ambiguities in the form of the relativistic NN scattering amplitudes by employing pseudovector coupling for the  $\pi$ NN vertex. In Ref. [1], Horowitz and Murdock have shown that the tensor potential has a negligible effect on all the observables and nuclei of interest. In a similar vein and for comparison to the latter, we also neglect the small tensor term.

## B. Relativistic Horowitz-Love-Franey model (HLF)

The original Love-Franey model and its relativistic version, i.e., Horowitz-Love-Franey model, have been described in detail in Ref. [5, 9, 10, 11] and references therein. Here, we briefly allude to list some important formula and the fitting procedure at lower energy. Essentially HLF model parameterizes the complex relativistic amplitudes  $F^L(q, E)$  in terms of a set of  $N = 10$  meson exchanges in first-order Born approximation, such that both direct

and exchange NN (tree-level) diagrams are considered separately, that is:

$$F^L(q, E) = \frac{iM^2}{2E_c k_c} [F_D^L(q) + F_X^L(Q)], \quad (10)$$

where

$$F_D^L(q) = \sum_{i=1}^N \delta_{L,L(i)} \langle \vec{\tau}_1 \cdot \vec{\tau}_2 \rangle^{T_i} f^i(q) \quad (11)$$

$$F_X^L(Q) = (-1)^{T_{NN}} \sum_{i=1}^N C_{L(i),L} \langle \vec{\tau}_1 \cdot \vec{\tau}_2 \rangle^{T_i} f^i(Q). \quad (12)$$

Here  $T_i = (0,1)$  denotes the isospin of the  $i^{\text{th}}$  meson,  $T_{NN}$  refers to the total isospin of the two-nucleon system,  $\langle \vec{\tau}_1 \cdot \vec{\tau}_2 \rangle^{T_i}$  is 1 or -3 for different  $T_{NN}$  and  $T_i$ ,  $C_{L(i),L}$  is the Fierz matrix [12], and

$$f^i(x) = \frac{g_i^2}{x^2 + m_i^2} \left(1 + \frac{x^2}{\Lambda_i^2}\right)^{-2} - i \frac{\bar{g}_i^2}{x^2 + \bar{m}_i^2} \left(1 + \frac{x^2}{\bar{\Lambda}_i^2}\right)^{-2} \quad (13)$$

where  $x$  represents the magnitude of either the direct three-momentum transfer  $q$  or the exchange-momentum transfer  $Q$ ,  $(g_i^2, \bar{g}_i^2)$ ,  $(m_i, \bar{m}_i)$ , and  $(\Lambda_i, \bar{\Lambda}_i)$  are the real and imaginary parts of the coupling constant, mass, and cutoff parameter for the  $i^{\text{th}}$  meson. These parameters are obtained by fitting the theoretical amplitudes with the values extracted from the NN scattering data.

Recently we have developed a set of parameter at incident laboratory kinetic energies ranging from 40 to 300 MeV [5], in which the coupling constant is set as energy dependent, namely

$$g^2(E) = g_0^2 [1 + a_g (e^{a_T T_{\text{rel}}} - 1)] \quad (14)$$

where

$$T_{\text{rel}} \equiv \frac{T_0 - T_{\text{lab}}}{T_0} \quad (15)$$

with  $T_0 = 200$  MeV,  $T_{\text{rel}}$  is positive in the 50 to 200 MeV energy range of interest, and  $g_0^2$ ,  $a_g$  and  $a_T$  are dimensionless parameters extracted by fitting to the relevant data.

### C. Relativistic Mean Field theory (RMF)

For extracting the relevant scalar and vector proton and neutron densities to be folded with the HLF NN scattering matrix, we employ the so-called PK1 Lagrangian density [13],

namely

$$\begin{aligned}
\mathcal{L} = & \bar{\psi} \left[ i\gamma^\mu \partial_\mu - M - g_\sigma \sigma - g_\omega \gamma^\mu \omega_\mu - g_\rho \gamma^\mu \vec{\tau} \cdot \vec{\rho}_\mu - e\gamma^\mu A_\mu \frac{1 - \tau_3}{2} \right] \psi \\
& + \frac{1}{2} \partial_\mu \sigma \partial^\mu \sigma - \frac{1}{2} m_\sigma^2 \sigma^2 - \frac{1}{3} g_2 \sigma^3 - \frac{1}{4} g_3 \sigma^4 \\
& - \frac{1}{4} \Omega_{\mu\nu} \Omega^{\mu\nu} + \frac{1}{2} m_\omega^2 \omega_\mu \omega^\mu + \frac{1}{4} c_3 (\omega_\mu \omega^\mu)^2 \\
& - \frac{1}{4} \vec{R}_{\mu\nu} \vec{R}^{\mu\nu} + \frac{1}{2} m_\rho^2 \vec{\rho}_\mu \cdot \vec{\rho}^\mu \\
& - \frac{1}{4} F_{\mu\nu} F^{\mu\nu},
\end{aligned} \tag{16}$$

where the parameters are listed in Table I, and the field tensors for the vector mesons and the photon are respectively defined as,

$$\begin{cases} \Omega_{\mu\nu} = \partial_\mu \omega_\nu - \partial_\nu \omega_\mu, \\ \vec{R}_{\mu\nu} = \partial_\mu \vec{\rho}_\nu - \partial_\nu \vec{\rho}_\mu, \\ F_{\mu\nu} = \partial_\mu A_\nu - \partial_\nu A_\mu. \end{cases} \tag{17}$$

TABLE I: The PK1 effective interaction. The masses (in MeV), meson-nucleon couplings, and nonlinear coefficients are listed.

$M_n$	$M_p$	$m_\sigma$	$m_\omega$	$m_\rho$	$g_\sigma$	$g_\omega$	$g_\rho$	$g_2$	$g_3$	$c_3$
939.5731	938.2796	514.0891	784.254	763	10.3222	13.0131	4.5297	-8.1688	-9.9976	55.636

Under the variation of the Langrangian density with respect to the different fields, one obtains the equations of motion for the nucleon and different mesons via a self-consistent procedure. To obtain the parameters, the masses of spherical nuclei  $^{16}\text{O}$ ,  $^{40}\text{Ca}$ ,  $^{48}\text{Ca}$ ,  $^{56}\text{Ni}$ ,  $^{68}\text{Ni}$ ,  $^{90}\text{Zr}$ ,  $^{116}\text{Sn}$ ,  $^{132}\text{Sn}$ ,  $^{194}\text{Pb}$ , and  $^{208}\text{Pb}$ , the compression modulus  $K$ , the baryonic density at saturation  $\rho_{\text{sat}}$ , and the asymmetry energy  $J$  of nuclear matter are fitted to give the minimum by the Levenberg-Marquardt method. The relative deviations are 0.0102 and 0.0178 for the masses of 19 spherical nuclei and charge radii of 13 spherical nuclei, respectively, which are similar or better than the other commonly used RMF effective interactions, such as the NL1 [14], PL-40 [15], NL-SH [16], TM1 [17], NL3 [18], TW99 [19], and DD-ME1 [20]. Compared to these effective interactions, the PK1 parametrization represents an improvement in the sense that center-of-mass corrections are included microscopically and it also provides a unified description of the properties of stable and unstable nuclei over a broad mass ( $16 \leq A \leq 214$ ) range.

At last, to minimize uncertainties associated with nuclear structure input, we focus on proton scattering from  $^{208}\text{Pb}$  which is a spin-zero spherical nucleus for which the PK1 effective interaction can give excellent description. In Fig. 1, the scalar and vector density distributions for proton and neutron of  $^{208}\text{Pb}$  are shown. Another advantage for considering such a heavy nucleus as  $^{208}\text{Pb}$ , is that at the low energies of interest, recoil corrections to the Dirac scattering equation are expected to be small and hence can be neglected.

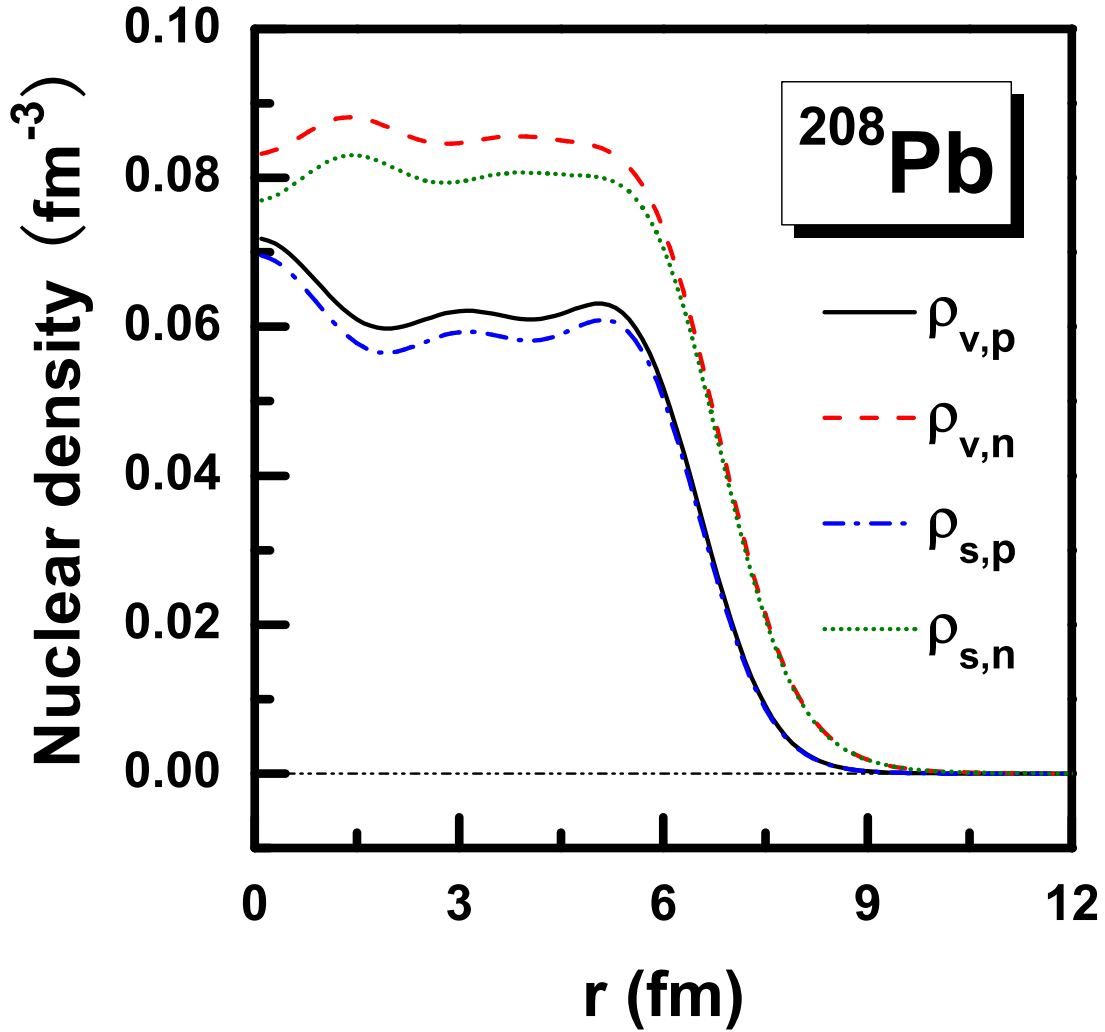


FIG. 1: (Color online) Scalar, and vector (baryon) density (in units of  $\text{fm}^{-3}$ ) distribution in radial direction  $r$  (in fm) for proton and neutron of  $^{208}\text{Pb}$ , respectively. The proton and neutron densities are denoted by solid and dashed curves, respectively. The dash dotted curve corresponds to the proton scalar density, and dotted curve indicates the neutron scalar density. The PK1 effective interaction is used.

### III. RESULTS

Guided by the availability of experimental data at the lower, middle and higher-energy regions of the 50 – 200 MeV range, we focus on incident energies of 65 [21], 98 [22], 121 [23] and 200 MeV [24, 25], and examine the validity of our RIA predictions for describing  $d\sigma/d\Omega$ ,  $A_y$  and  $Q$  from a  $^{208}\text{Pb}$  target nucleus as the energy is systematically lowered. Note that at approximately 100 MeV, there exists no complete set of experimental data for one specific energy, and hence we compare our RIA calculations (in the mid-energy range) to data for  $d\sigma/d\Omega$  and spin observables,  $A_y$  and  $Q$ , at 121 MeV and 98 MeV, respectively.

In Figs. 2, 3, and 4, the RIA calculations are denoted by black dashed curves (color red online) and for reference we also display results based on the energy-dependent mass-independent (EDAI) global Dirac optical potentials (GOP) [2] indicated by the black dotted curves (color olive online). We consider center-of-mass scattering angles ranging up to a maximum value corresponding to a three-momentum transfer of about  $q \approx 2.5 \text{ fm}^{-1}$  for which first-order microscopic nonrelativistic models and relativistic global optical potentials have been shown to be valid [26]. As expected, the global Dirac optical potentials provide an excellent description of all the observables for the entire energy range of interest. At 200 MeV, the RIA provides a satisfactory description of  $d\sigma/d\Omega$  and  $A_y$  for angles ranging up to a value corresponding to the third minimum in  $d\sigma/d\Omega$ . Although the RIA provides a good description of  $Q$  from 20 to 40 degrees, it fails to describe the small angle behavior. At lower energies, the RIA provides a satisfactory description of  $d\sigma/d\Omega$  up to approximately the second minimum, but fails to describe  $A_y$  and  $Q$ .

For elastic proton scattering from a heavy nucleus such as  $^{208}\text{Pb}$ , Murdock and Horowitz [1] have demonstrated that Pauli Blocking (PB) corrections to the RIA optical potentials play an increasingly significant role at lower energies. Essentially PB represents the mechanism that prevents nucleons in the nuclear medium from scattering to occupied intermediate states [27]. We now proceed to study the effect of PB corrections for our low energy range of interest. Following the procedure outlined in Ref. [1], we include PB corrections to the RIA microscopic optical potentials via the so-called energy-dependent PB coefficients  $a_{S,V}(T_{\text{lab}})$ , that is,

$$U_{\text{PB}}^{S,V}(r, T_{\text{lab}}) = \left[ 1 - a_{S,V}(T_{\text{lab}}) \left( \frac{\rho_B(r)}{\rho_0} \right)^{2/3} \right] U^{S,V}(r, T_{\text{lab}}) \quad (18)$$



where  $T_{\text{lab}}$  denotes the incident laboratory kinetic energy,  $\rho_B(r)$  is the local RMF baryon density of the target nucleus,  $\rho_0 = 0.1934 \text{ fm}^{-3}$ , and  $U^{S,V}(r, T_{\text{lab}})$  represents the uncorrected RIA scalar  $S$  and vector  $V$  optical potentials. Within the context of a relativistic Dirac-Brueckner approach, values for the PB correction factors  $a_{S,V}(T_{\text{lab}})$  have been extracted at discrete energies of 135, 200, 300 and 400 MeV [1] and also at discrete momenta ranging from about 0.46 to 0.75 GeV/c [28]. Consistent with the results reported in Ref. [1], in Fig. 2 we confirm that PB corrections (black solid curve) provide an improved description of the 200 MeV data, the effect been most pronounced for  $A_y$  and  $Q$  at small angles. Due to the enhanced sensitivity exhibited by spin observables, we now focus on the influence of PB on  $A_y$  at a lower energy of 98 MeV, where PB corrections are expected to be more significant: note that there are no experimental data for  $Q$  at 98 MeV. The lack of published PB coefficients at this energy necessitates linear extrapolation of the published Dirac-Brueckner values in Ref. [1], which is shown in Fig. 5. RIA predictions with and without PB corrections are denoted by the gray solid (color cyan online) and black dashed (color red online) curves in Fig. 6 (a), respectively. One clearly observes that the extrapolated Dirac-Brueckner PB corrections cannot account for the  $A_y$  data.

Due to the latter failure, we now proceed to study PB via a phenomenological approach. In particular, we study to which extent phenomenologically extracted values of  $a_{S,V}(T_{\text{lab}})$  can provide a consistent description of complete sets of scattering observables at the specific energies of interest. Starting with the lower momentum values of  $a_{S,V}(T_{\text{lab}})$  published in table 2 [ $\rho_0$ ,  $p = 0.46 \text{ GeV}/c$ ] of Ref. [28], we systematically vary the real and imaginary parts to give one GOP that provides the best fit-by-eye of  $d\sigma/d\Omega$ ,  $A_y$  and  $Q$  for elastic proton scattering from  $^{208}\text{Pb}$  at five discrete energies of 65, 100, 135, 170 and 200 MeV, spanning the range of interest. In fact, this is enough for the purpose of this paper: to check the validity of the RIA at lower energies. Our phenomenological PB factors are listed in Table II together with the corresponding published Dirac-Brueckner values from Ref. [1].

We now consider the effect of these phenomenological corrections on  $A_y$  at 98 MeV, where the extrapolated Dirac-Brueckner corrections were shown to fail. In Fig. 6 (a) one clearly sees that our phenomenological PB corrections (black solid curve) provide a more satisfactory description of  $A_y$  compared to the Dirac-Brueckner PB corrections (gray solid curve). Focusing on the optical potentials, in Fig. 6 (b) we observe that the main effect of both Dirac-Brueckner (grey solid curves) and phenomenological (black solid curves) PB is

TABLE II: Phenomenological Pauli blocking correction factors  $a(T_{\text{lab}})$  for real and imaginary RIA microscopic scalar  $S$  and vector  $V$  optical potentials as various energies  $T_{\text{lab}}$ . Where available, the corresponding published Dirac-Brueckner values [1] are indicated in square brackets.

Energy [MeV]	Scalar		Vector	
	Real	Imaginary	Real	Imaginary
65	0.020	0.68	0.14	0.85
100	0.007	0.60	0.11	0.73
135	0.005 [0.00377]	0.53 [0.108825]	0.09 [0.08403]	0.60 [0.24535]
170	0.008	0.42	0.07	0.50
200	0.010 [-0.0078]	0.35 [0.098]	0.0605 [0.0605]	0.42 [0.207]

to decrease the strengths of the real and imaginary parts of the scalar and vector optical potentials, the effect being most pronounced for the imaginary parts. Furthermore, our phenomenological corrections have a larger effect than the corresponding Dirac-Brueckner corrections. Also note that the PB-corrected optical potentials differ in strength from the corresponding global optical potentials (black dotted curve), which suggests that the delicate interplay between the relative strengths and signs of the scalar and vector optical potentials, rather than absolute magnitudes, is responsible for providing an accurate description of the diffractive behavior of all scattering observables.

In Figs. 2, 3, and 4, we now display our theoretical predictions including the above-mentioned phenomenological PB corrections (black solid curves) over the entire range of interest. Although not shown, both Dirac-Brueckner and phenomenological PB corrections provide the same quantitative improvement for all observables at 200 MeV. At 121 MeV, PB corrections provide an excellent description of the first few maxima and minima for  $d\sigma/d\Omega$ . There are no data for  $Q$  at 98 MeV, but we note that PB corrections give results very similar to the corresponding global Dirac optical potentials. At the lower energy of 65 MeV, PB corrections invoke a larger effect and provide a satisfactory description of  $d\sigma/d\Omega$  and  $A_y$  up to about 50 degrees, but predictions deteriorate at larger angles. Note, however, that at 65 MeV, PB corrections fail to quantitatively describe the first two extrema for  $A_y$ , as well as fail to reproduce  $Q$  over the entire angular range. The 65 MeV results emphasize the important fact that optical potentials can be deemed reliable only if complete sets of elastic

scattering observables, as opposed to only one or two observables, are accurately described.

To further validate our phenomenological procedure for including PB corrections, in Fig. 7 we now consider a different spin-zero spherical target nucleus, namely  $^{40}\text{Ca}$ , at an incident proton energy of 152 MeV: the meaning of the various curves is the same as those in Fig. 2. Compared to the observables without PB (black dashed curves), and consistent with our conclusions for  $^{208}\text{Pb}$ , the corrected values (black solid curves) provide an improved description of all observables and also agree with the GOP results.

Although PB systematically improves the RIA predictions at lower energies, these corrections do not provide a quantitative description of complete sets of observables, and hence it is clear that other effects also begin to play an increasingly significant role as the energy is lowered. The question now arises as to whether one can incorporate additional corrections so as to consistently improve these low energy results within the framework of the RIA. Various authors [4, 30, 31] have stressed that importance of nuclear medium modifications to the NN interaction at lower energies. In particular, a number of theoretical models [13, 32, 33, 34] predict density-dependent corrections to meson-nucleon coupling constants as well as nucleon- and meson-masses in normal nuclear matter. We now adopt a phenomenological approach to investigate to what extent the renormalization of certain meson-nucleon coupling constants can provide a systematic improvement of the data at 65 MeV. Since scalar and vector RIA optical potentials are dominated by contributions from  $\sigma$ - and  $\omega$ -meson exchange to the NN scattering amplitudes, we vary the values of the real  $\sigma\text{N}$  and  $\omega\text{N}$  coupling constants,  $g_\sigma^2$  and  $g_\omega^2$ , so as to provide the best consistent description of elastic proton-nucleus scattering. The result of this procedure is that the value of  $g_\sigma^2$  changes from -7.5701 to -11.1734 and  $g_\omega^2$  changes from 7.4511 to 12.9704: these new values of the couplings correspond to  $a_g = 0.0271$  and  $a_T = 3.8364$  for the  $\sigma$  meson and to  $a_g = 0.1022$  and  $a_T = 1.9527$  for the  $\omega$  meson [see Eq. (14) in this paper, also Eq. (21) and Table II in Ref. [5]]. The effect of renormalizing these couplings is illustrated by comparing the original results (black solid curves) to the renormalized values (gray solid curve) in Fig. 4. The most pronounced improvement is observed for the minima of  $d\sigma/d\Omega$  at large scattering angles and spin observables at small scattering angles. At the level of the optical potentials, the main effect of the modified coupling constants is to increase the strengths of the real parts of the scalar and vector potentials at lower energies such that the energy-dependent trend these strengths is qualitatively similar to the corresponding GOP results, as illustrated in Fig. 8.

Furthermore, these improved predictions arising from renormalized coupling constants are consistent with other nuclear reaction- and structure-studies focusing on density-dependent corrections to the NN interaction [13, 30, 31, 35]. Note, however, that the best description of  $A_y$  and  $Q$  up to angles of about 40 degrees, is obtained by including *both* PB and density-dependent corrections (gray solid curve).

To further test the consistency of our scheme for including *both* PB and density-dependent corrections, we now focus on elastic proton scattering at an energy as low as 30 MeV where these effects are expected to be important. In Fig. 9, it is gratifying to observe that both phenomenological corrections (gray solid curves) contribute significantly toward providing an excellent description of the  $d\sigma/d\Omega$  and  $A_y$  data [36, 37] over the entire angular region. Although there are no data for  $Q$  at this energy, we note that our predictions are similar to the GOP results which have constrained to fit elastic scattering observables at energies as low as 20 MeV [2]. The above mentioned results inspire confidence in the predictive power of our phenomenological corrections to the RIA.

Finally, we check the validity of the RIA model for describing total reaction cross section  $\sigma_R$  data for proton scattering from  $^{208}\text{Pb}$  for energies lower than 200 MeV. This integral quantity serves as crucial input in designing accelerator-driven-systems for transmutation of radioactive waste. However, due to the shortage of relevant  $\sigma_R$  data, simulations are forced to employ model-dependent values as input [38]. Furthermore,  $\sigma_R$  values also form an essential ingredient in studies of nuclearsynthesis and stellar evolution. Consequently, the need for developing predictive models of elastic proton scattering should be evident. In Fig. 10 we observe that compared to the uncorrected RIA predictions, denoted by the black dashed line (color red online), the inclusion of both PB and density-dependent corrections, indicated by the gray solid line (color cyan online), provides a satisfactory description of the data: the experimental data are from Refs. [39, 40, 41, 42, 43, 44, 45, 46]. Our results are consistent with corresponding nonrelativistic microscopic predictions [26] as well as the GOP values (black dotted curve), over the entire energy range. In particular, both RIA and nonrelativistic models fail to describe the 70 MeV data: a point of concern, however, is the unsystematic trend exhibited by the data in this region, as already mentioned in Ref. [26].

#### IV. SUMMARY AND CONCLUSIONS

We present the first study to examine the validity of the relativistic impulse approximation (RIA) for describing elastic proton-nucleus scattering at incident laboratory kinetic energies lower than 200 MeV. For simplicity we considered a  $^{208}\text{Pb}$  target, which is a spin-zero spherical nucleus for which accurately calibrated relativistic mean field nuclear structure models exist, and for which recoil corrections to the Dirac scattering equation are expected to be negligible. Microscopic scalar and vector optical potentials are generated by folding our recently developed relativistic meson-exchange model of the NN scattering matrix with appropriate Lorentz densities arising from the PK1 Lagrangian density. We have established that phenomenological Pauli blocking effects and density-dependent corrections to the  $\sigma\text{N}$  and  $\omega\text{N}$  meson-nucleon coupling constants modify the RIA microscopic scalar and vector optical potentials so as to provide a consistent and quantitative description of all elastic scattering observables ( $\sigma_R$ ,  $d\sigma/d\Omega$ ,  $A_y$  and  $Q$ ) at energies ranging from 30 to 200 MeV. In particular, the effect of PB becomes more significant at energies lower than 200 MeV, whereas phenomenological density-dependent corrections to the NN interaction *also* play an increasingly important role at energies lower than 100 MeV. Note that although our initial study has been of a phenomenological nature, our results clearly indicate the importance of including PB and density-dependent corrections to the microscopic RIA model for providing consistent and quantitative predictions of all of the above-mentioned scattering observables at energies lower than 200 MeV. Indeed the latter conclusion is consistent with corresponding nonrelativistic microscopic studies [4, 26]. Guided by our phenomenological result, the next phase will be to incorporate the PB and density-dependent corrections within the context of microscopic relativistic dynamical models in a manner similar to the successful nonrelativistic  $g$ -folding model developed by the Melbourne group [47].

In closing, we emphasize that not only is the RIA a highly predictive model, but it also provides a microscopic meson-exchange picture for understanding the behavior of the successful global Dirac optical potentials. Another attractive feature of the RIA is the consistent application of the relativistic meson-exchange NN scattering matrix for generating microscopic folding optical potentials – required for calculating the scattering wave functions necessary for evaluating relativistic transition matrix elements – and also for describing the driving NN reaction mechanism in relativistic distorted wave models of nucleon-induced

reactions. One of the most useful applications envisaged for the RIA will be to generate microscopic optical potentials for studying elastic and inelastic scattering of nucleons from unstable neutron- and proton-rich nuclei for which global optical potentials do not exist. Indeed, existing global Dirac optical potentials have been constrained to reproduce elastic proton scattering from stable nuclei [2], and hence there is no reason to believe that these potentials can be reliably extrapolated for studies of exotic nuclei. On the other hand, one can readily extend the RIA folding procedure to calculate microscopic optical potentials for exotic nuclei. The latter can easily be realized due to the current availability of suitable relativistic meson-exchange models [5, 48, 49] as well sophisticated relativistic mean field nuclear structure models for unstable nuclei [50, 51]. Future work will focus on studying elastic proton scattering from exotic nuclei.

This work is partly supported by the Major State Basic Research Developing Program 2007CB815000, the National Natural Science Foundation of China under Grant Nos. 10435010, 10775004 and 10221003, as well as the National Research Foundation of South Africa under Grant No. 2054166.

- 
- [1] D. P. Murdock and C. J. Horowitz, *Phys. Rev. C* **35**, 1442 (1987).
  - [2] E. D. Cooper, S. Hama, B. C. Clark, and R. L. Mercer, *Phys. Rev. C* **47**, 297 (1993).
  - [3] P. K. Deb and K. Amos, *Phys. Rev. C* **62**, 024605 (2000).
  - [4] P. K. Deb, K. Amos, and S. Karataglidis. *Phys. Rev. C* **62**, 037601 (2000).
  - [5] Z. P. Li, G. C. Hillhouse, and J. Meng, *Phys. Rev. C* **77**, 014001 (2008).
  - [6] C. R. Chinn, Ch. Elster, R. M. Thaler, and S. P. Weppner, *Phys. Rev. C* **51**, 1418 (1995).
  - [7] E. J. Stephenson, R. C. Johnson, and F. Sammarruca, *Phys. Rev. C* **71**, 014612 (2005).
  - [8] C. J. Horowitz, D. P. Murdock, and B. D. Serot, in *Computational Nuclear Physics I*, edited by K. Langanke, J. A. Maruhn, and S. E. Koonin (Springer-Verlag, Berlin, 1991), p. 129
  - [9] W. G. Love and M. A. Franey, *Phys. Rev. C* **24**, 1073 (1981).
  - [10] M. A. Franey and W. G. Love, *Phys. Rev. C* **31**, 488 (1985).
  - [11] C. J. Horowitz, *Phys. Rev. C* **31**, 1340 (1985).
  - [12] M. Fierz, *Z. Phys.* **104**, 533 (1937).
  - [13] Wenhui Long, Jie Meng, Nguyen Van Giai and Shan-Gui Zhou, *Phys. Rev. C* **69** (2004)

034319.

- [14] P. G. Reinhard, M. Rufa, J. Maruhn, W. Greiner and J. Friedrich, *Z. Phys. A* **323**, 13 (1986).
- [15] P. G. Reinhard, *Z. Phys. A* **329**, 257 (1988).
- [16] M. M. Sharma, M. A. Nagarajan and P. Ring, *Phys. Lett.* **B312**, 377 (1993).
- [17] Y. Sugahara and H. Toki, *Nucl. Phys.* **A579**, 557 (1994).
- [18] G. A. Lalazissis, J. Konig and P. Ring, *Phys. Rev. C* **55**, 540 (1997).
- [19] S. Typel and H. H. Wolter, *Nucl. Phys.* **A656**, 331 (1999).
- [20] T. Niksic, D. Vretenar, P. Finelli and P. Ring, *Phys. Rev. C* **66**, 024306 (2002).
- [21] H. Sakaguchi, *et al.*, *Phys. Rev. C* **26**, 944 (1982).
- [22] A. Nadasen, *et al.*, *Phys. Rev. C* **23**, 1023 (1981).
- [23] P. Schwandt, *et al.*, *Phys. Rev. C* **26**, 55 (1982).
- [24] D. A. Hutcheon, *et al.*, *Nucl. Phys.* **A483**, 429 (1988).
- [25] N. Ottenstein, *et al.*, *Phys. Rev. C* **38**, 2272 (1988), and references therein.
- [26] P. K. Deb, B. C. Clark, S. Hama, K. Amos, S. Karataglidis and E. D. Cooper, *Phys. Rev. C* **72**, 014608 (2005).
- [27] M. I. Haftel and F. Tabakin, *Nucl. Phys.* **A158**, 1 (1970).
- [28] Bernard Ter Haar and Rudi Malfliet, *Phys. Lett.* **B172**, 10 (1986).
- [29] C. Rolland, *et al.*, *Nucl. Phys.* **80**, 625 (1966).
- [30] H. Sakaguchi, *et al.*, *Phys. Rev. C* **57**, 1749 (1998).
- [31] G. C. Hillhouse, J. Mano, S. M. Wyngaardt, B. I. S van der Ventel, T. Noro, and K. Hatanaka, *Phys. Rev. C* **68**, 034608 (2003).
- [32] B. D. Serot and J. D. Walecka, in *Advances in Nuclear Physics*, edited by J. W. Negele and E. Vogt (Plenum Press, New York, 1986), Vol. 16, p. 116.
- [33] G. E. Brown and M. Rho, *Phys. Rev. Lett.* **66**, 2720 (1991).
- [34] R. J. Furnstahl, D. K. Griegel and T. D. Cohen, *Phys. Rev. C* **46**, 1507 (1992).
- [35] G. C. Hillhouse and T. Noro, *Phys. Rev. C* **74**, 064608 (2006).
- [36] W. T. H. Van Oers, *et al.*, *Phys. Rev. C* **10**, 307 (1974).
- [37] B. W. Ridley and J. F. Turner, *Nucl. Phys.* **58**, 497 (1964).
- [38] P. K. Deb, K. Amos, S. Karataglidis, M. B. Chadwick, and D. G. Madland, *Phys. Rev. Lett.* **86**, 3248 (2001).
- [39] T. J. Gooding, *Nucl. Phys.* **12**, 241 (1959).

- [40] V. Meyer, R. M. Eisberg, and R. F. Carlson, Phys. Rev. **117**, 1334 (1960).
- [41] R. Goloskie and K. Strauch, Nucl. Phys. **29**, 474 (1962).
- [42] P. Kirkby and W. T. Link, Can. J. Phys. **44**, 1847 (1966).
- [43] J. J. H. Menet, E. E. Gross, J. J. Malanify, and A. Zucker, Phys. Rev. C **4**, 1114 (1971).
- [44] R. F. Carlson, *et al.*, Phys. Rev. C **12**, 1167 (1975).
- [45] A. Ingemarsson, *et al.*, Nucl. Phys. **A653**, 341 (1999).
- [46] A. Auce, A. Ingemarsson, R. Johansson, M. Lantz, G. Tibell, R. F. Carlson, M. J. Shachno, A. A. Cowley, G. C. Hillhouse, N. M. Jacobs, J. A. Stander, J. J. van Zyl, S. V. Förtsch, J. J. Lawrie, F. D. Smit, and G. F. Steyn, Phys. Rev. C **71**, 064606 (2005).
- [47] K. Amos, P. J. Dortmans, H. V. von Geramb, S. Karataglidis, and J. Raynal, Adv. Nucl. Phys. **25**, 275 (2000).
- [48] O. V. Maxwell, Nucl. Phys. **A600**, 509 (1996).
- [49] O. V. Maxwell, Nucl. Phys. **A638**, 747 (1998).
- [50] B. G. Todd and J. Piekarewicz, Phys. Rev. C **67**, 044317 (2003).
- [51] J. Meng, H. Toki, S. G. Zhou, S. Q. Zhang, W. H. Long and L. S. Geng. Prog. Part. Nucl. Phys. **57**, 470 (2006).



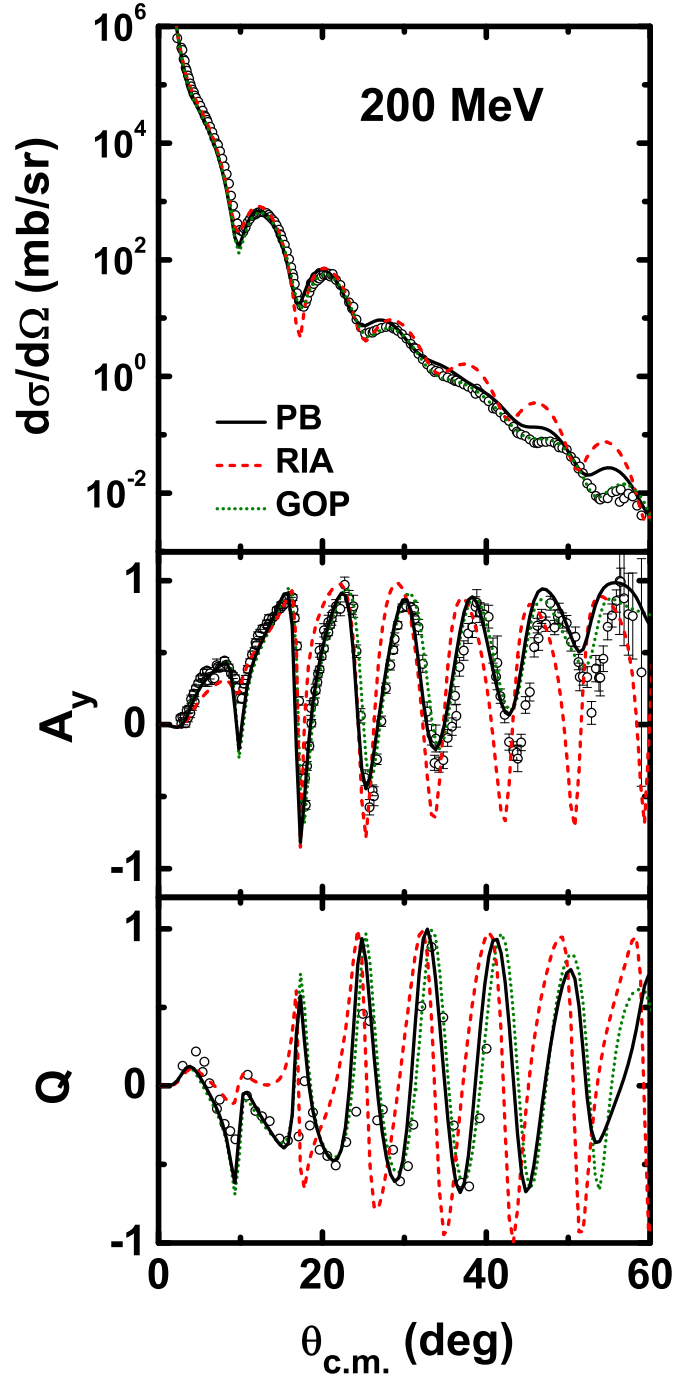


FIG. 2: (Color online) Differential cross sections  $d\sigma/d\Omega$  (in units of  $mb/sr$ ), analyzing powers  $A_y$  and spin rotation functions  $Q$ , plotted as a function of center-of-mass scattering angles  $\theta_{c.m.}$  (in degrees), for elastic proton scattering from  $^{208}\text{Pb}$  at incident laboratory kinetic energy of 200 MeV. The experimental data [24, 25] are denoted by open circles. Uncorrected RIA predictions are represented by black dashed curves (legend: RIA; color red online), the black dotted curves correspond to predictions based on the EDAI Dirac global optical potentials (GOP) [2] (legend: GOP; color olive online), and RIA calculations including phenomenological Pauli blocking (PB) corrections are indicated by the black solid curves (legend: PB).

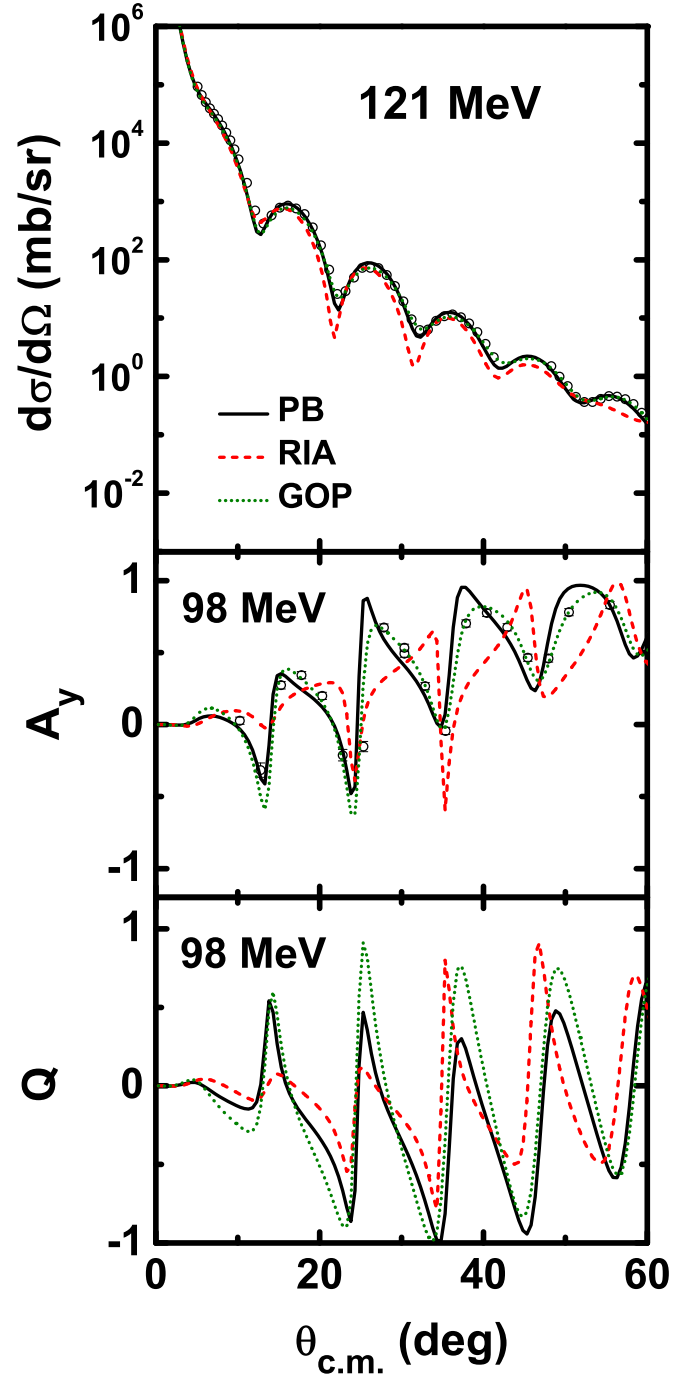


FIG. 3: (Color online) Same as Fig. 2, except for incident laboratory kinetic energies of 121 or 98 MeV. The experimental data at 121 [23] and 98 [22] are denoted by open circles.

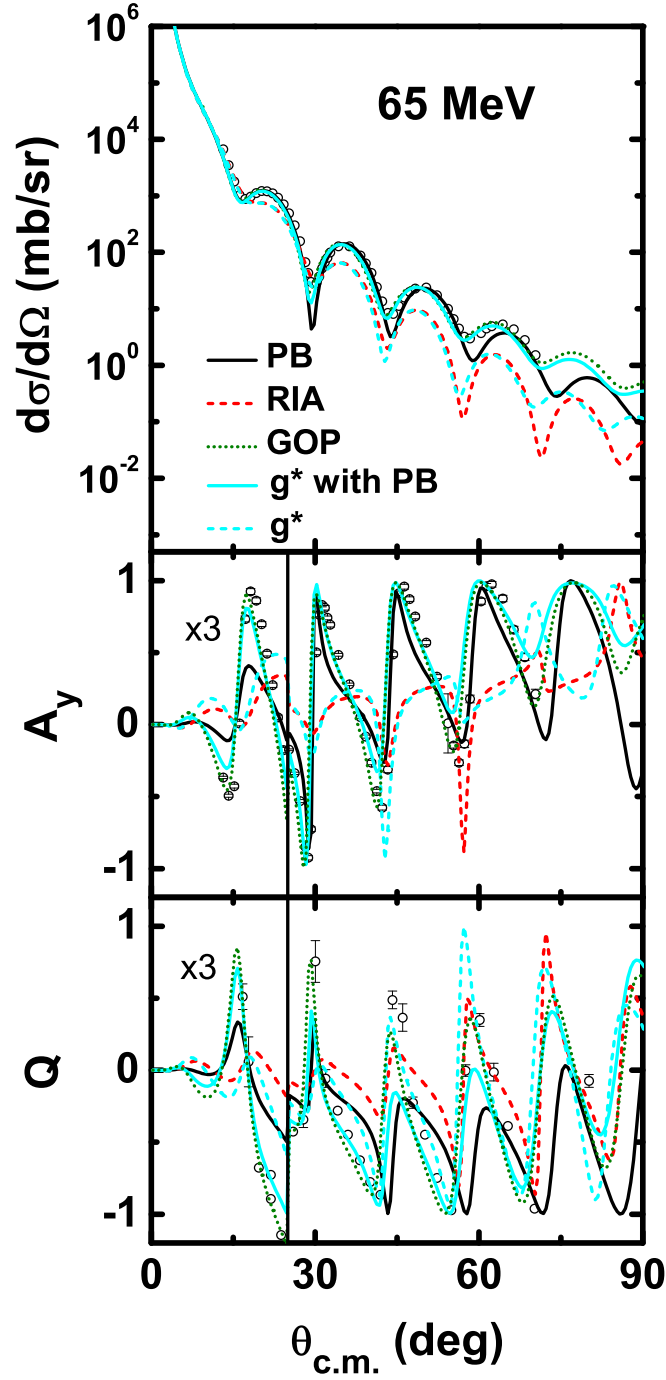


FIG. 4: (Color online) Same as Fig. 2, except for an incident laboratory kinetic energy of 65 MeV. The gray dashed curve (color cyan online) corresponds to RIA predictions based on the renormalized medium-modified  $\sigma N$  and  $\omega N$  coupling constants (denoted by the legend:  $g^*$ ), and the gray solid lines (color cyan online) denote the combined effect of medium modified coupling constants together with PB corrections (legend:  $g^*$  with PB). The experimental data [21] are denoted by open circles. The analyzing powers  $A_y$  and spin rotation functions  $Q$  are multiplied by 3 at the  $\theta_{c.m.}$  angles from 0 to 25 degrees.

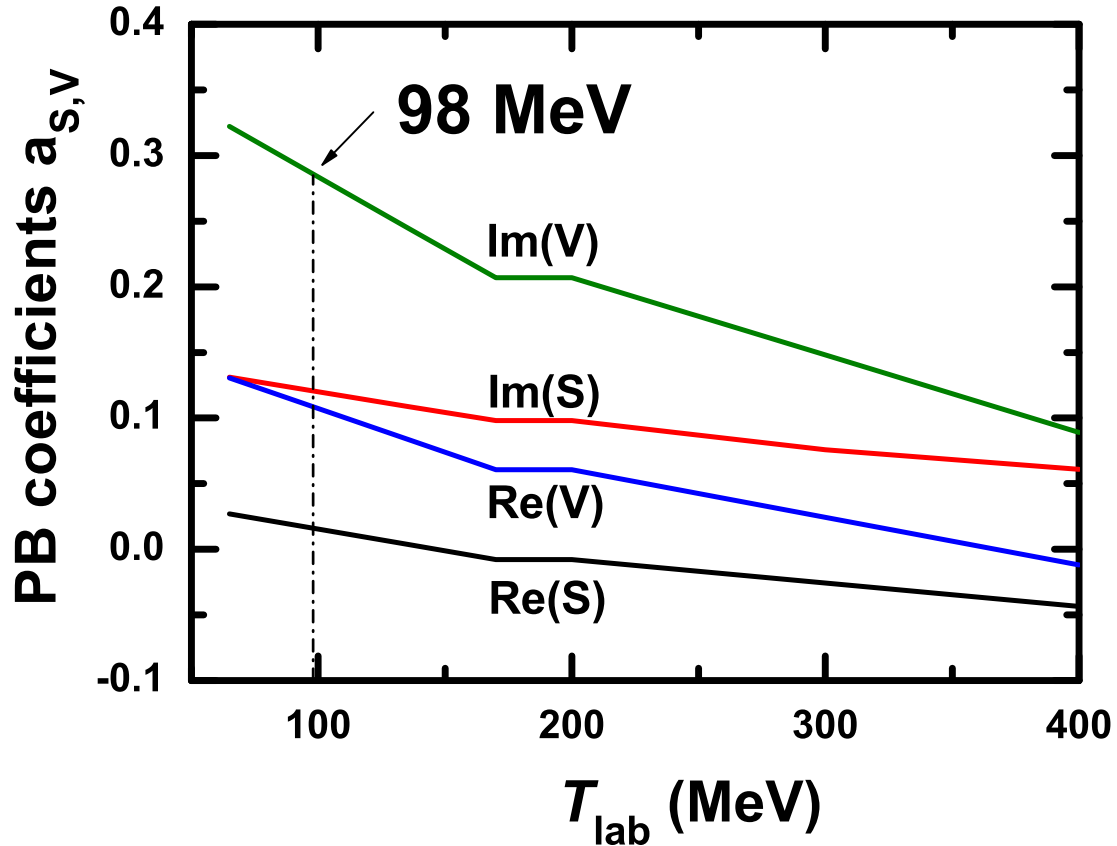


FIG. 5: (Color online) Linear interpolation and extrapolation of PB correction factors calculated from a relativistic Dirac-Brueckner approach. The four curves from top to bottom indicate the PB correction factors corresponding to the imaginary (Im) and real (Re) parts of the vector  $V$  and scalar  $S$  optical potentials. In the code corresponding to Ref. [8], the values at  $T_{\text{lab}} = 170$  MeV are chosen same as  $T_{\text{lab}} = 200$  MeV, which causes the flat section in the curves. The linear extrapolation at  $T_{\text{lab}} = 98$  MeV is emphasized.

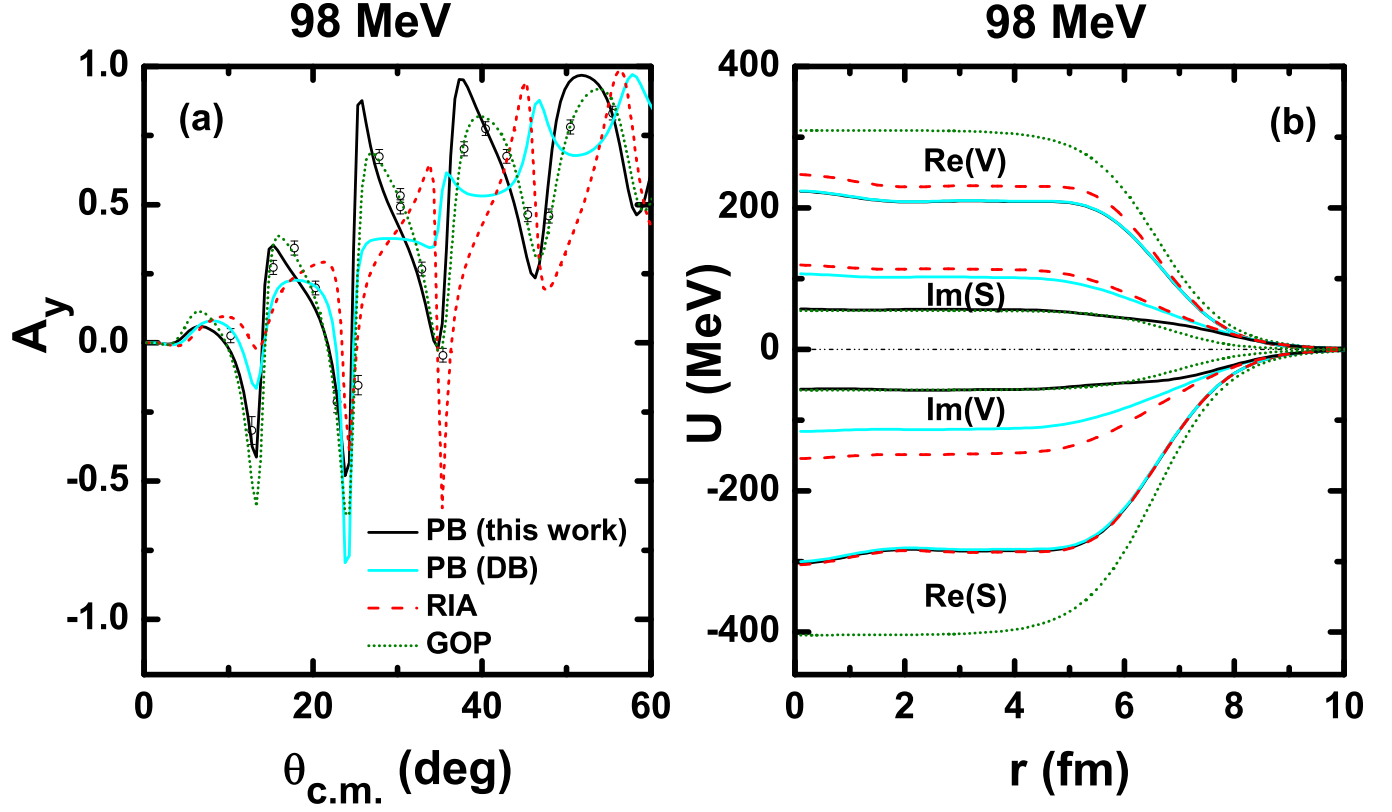


FIG. 6: (Color online) (a) Analyzing power  $A_y$  for elastic proton scattering from  $^{208}\text{Pb}$  at 98 MeV, plotted as a function of center-of-mass scattering angles  $\theta_{c.m.}$  (in degrees). The experimental data are taken from Ref. [22]. Uncorrected RIA predictions are represented by black dashed curves (legend: RIA; color red online), the black dotted curves (color olive online) correspond to predictions based on the EDAI Dirac global optical potentials (GOP) [2] (legend: GOP), and RIA calculations including extrapolated Dirac-Brueckner and phenomenological PB corrections are denoted by gray [legend: PB (DB); color cyan online] and black solid curves [legend: PB (this work)], respectively. (b) The corresponding real (Re) and imaginary (Im) scalar  $S$  and vector  $V$  optical potentials (in units of MeV) for elastic proton scattering from  $^{208}\text{Pb}$  at 98 MeV, plotted as a function of the nuclear radius  $r$  (in units of fm). In particular, the two black solid curves corresponding to the real parts of the scalar and vector optical potentials are covered by the gray curves.

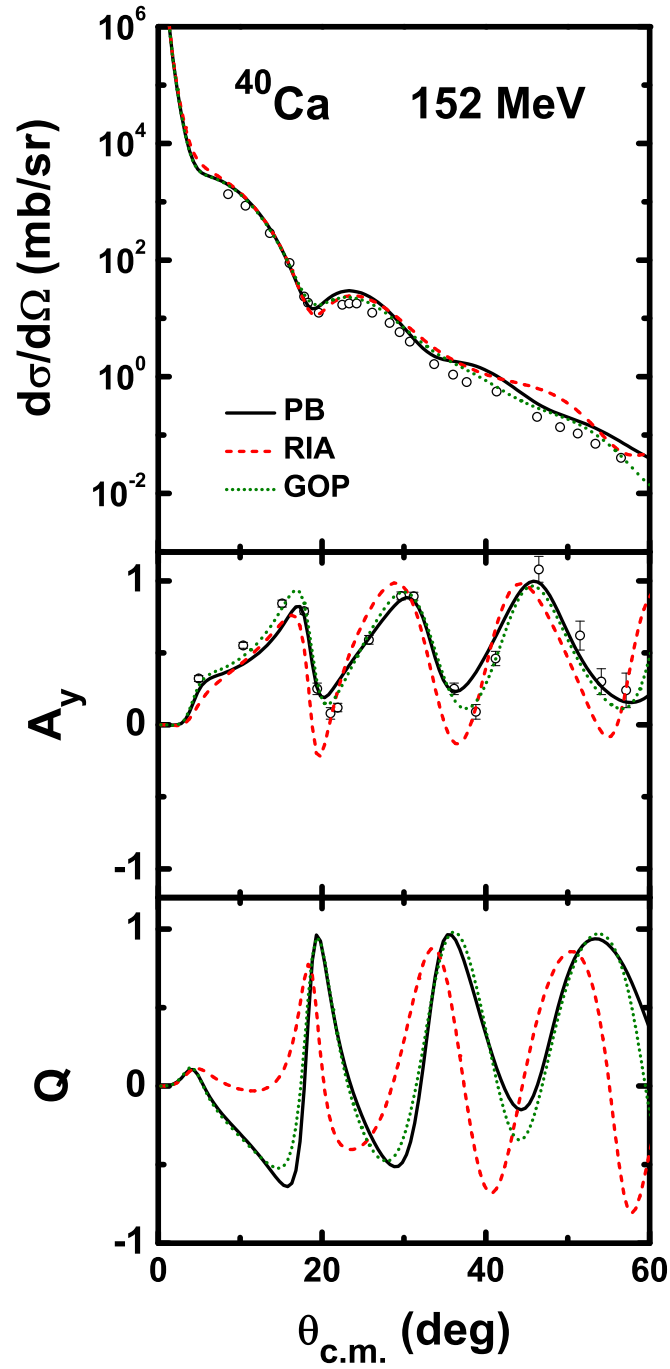


FIG. 7: (Color online) Same as Fig. 2, except for elastic proton scattering from  $^{40}\text{Ca}$  at incident laboratory kinetic energy of 152 MeV. The experimental data at 152 MeV are taken from Ref. [29].

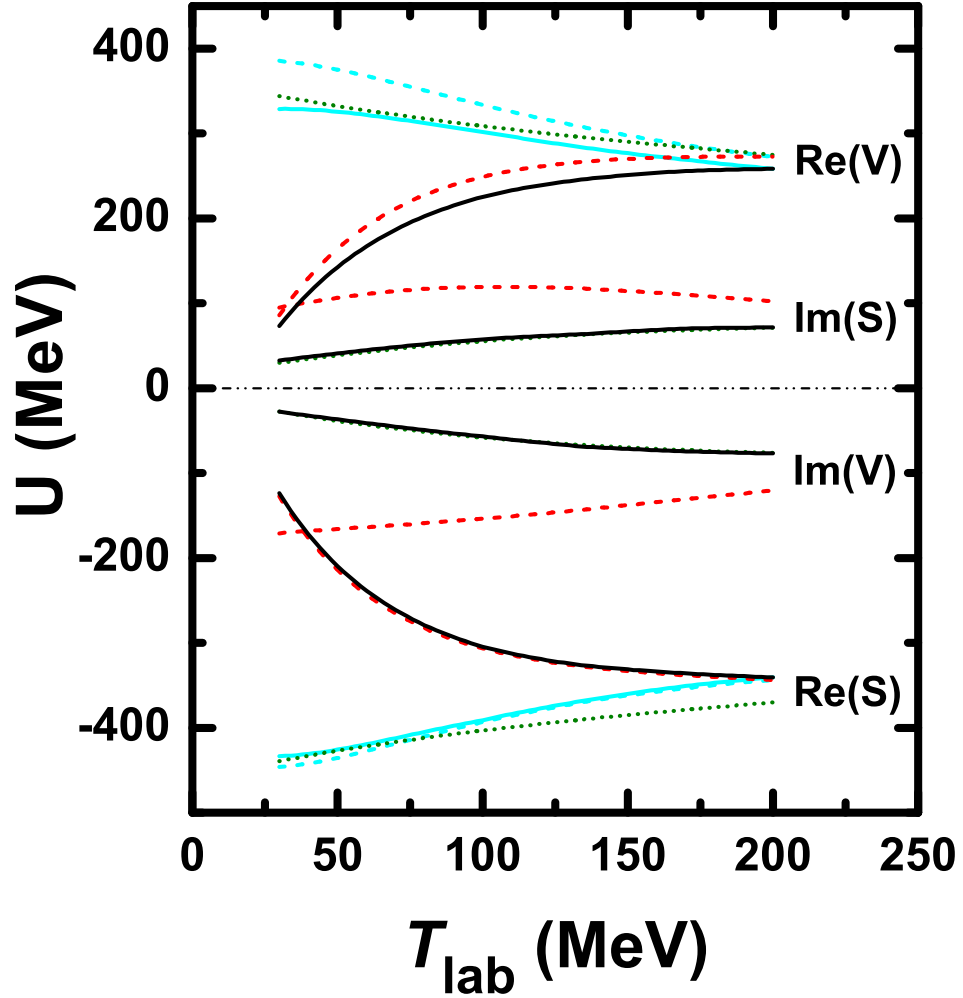


FIG. 8: (Color online) Strengths of the real (Re) and imaginary (Im) scalar  $S$  and vector  $V$  optical potentials (in units of MeV) at the center (radius  $r = 0$ ) of a  $^{208}\text{Pb}$  nucleus as a function of incident laboratory kinetic energies  $T_{\text{lab}}$  (in units of MeV). The identification of the curves is the same as in Fig. 4.

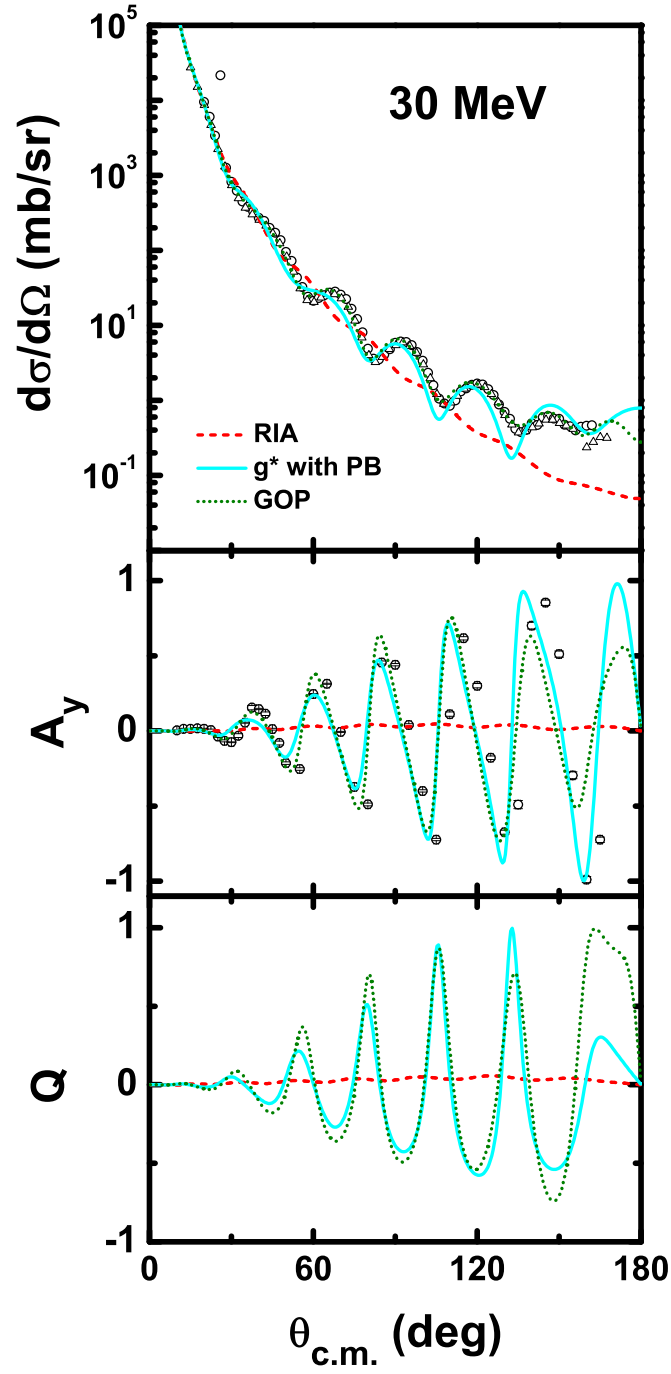


FIG. 9: (Color online) Same as Fig. 4, except for an incident laboratory kinetic energy of 30 MeV. The experimental data are taken from Ref. [36, 37].



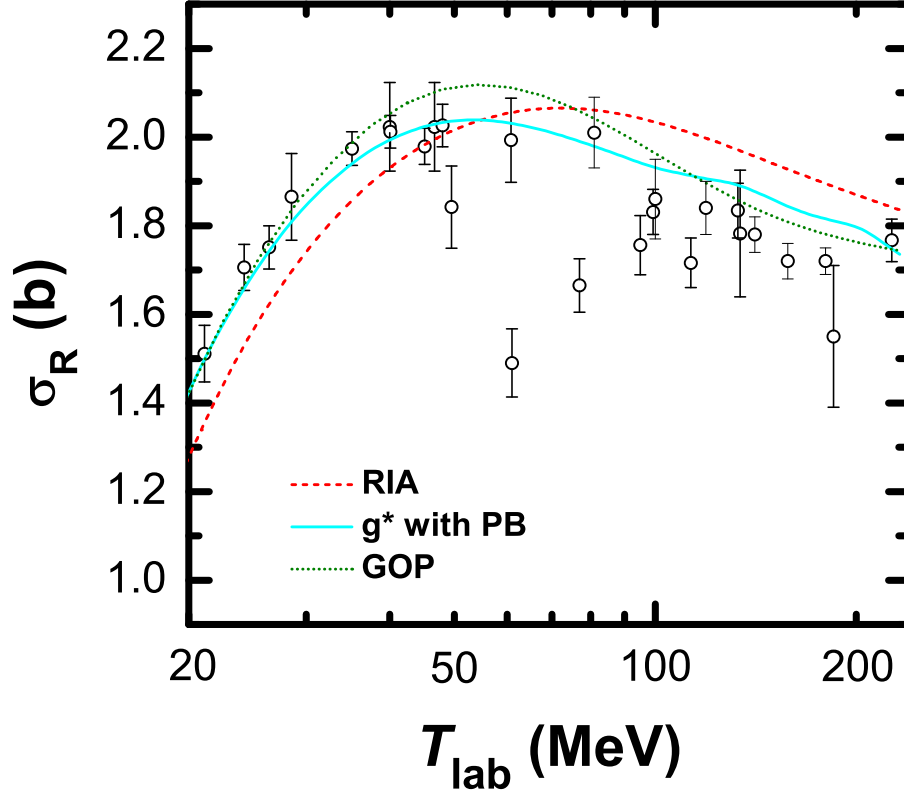


FIG. 10: (Color online) The total reaction cross section  $\sigma_R$  (in units of  $b$ ) for elastic proton scattering from  $^{208}\text{Pb}$  versus the incident laboratory kinetic energy  $T_{\text{lab}}$  (in units of MeV). The identification of the curves is the same as in Fig. 4. The experimental data are taken from Refs. [39, 40, 41, 42, 43, 44, 45, 46].